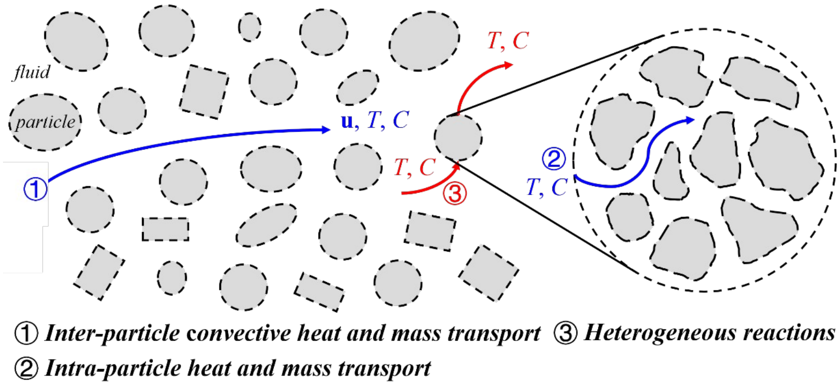

Fig. 1. Schematic diagram of reaction and heat and mass transport in porous media

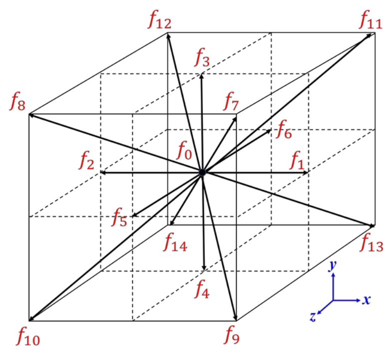

Fig. 2. Thematic diagram of D3Q15 discrete velocities model

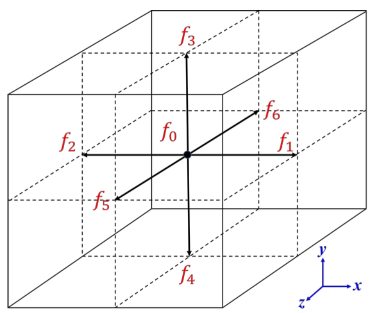

Fig. 3. Thematic diagram of D3Q7 discrete velocities model

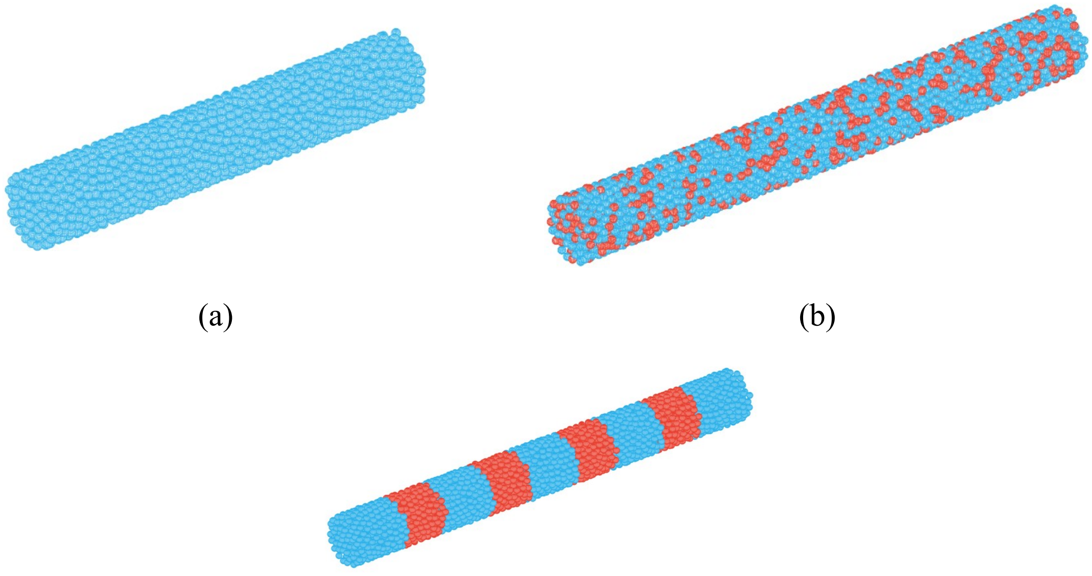

(a) (b)

(c)

Fig. 4. The schematic diagrams of the packing structure with the same number of catalyst particle (N_{cat}=2970) by the DEM approach: (a) Packing structure without inert particles (ε =0.488, d_{cat}=3.67 mm); (b) Catalyst uniformly mixed with inert particle (ε=0.490, d_{cat}=3.67 mm, N_{inert}/N_{cat}=1/2); (c) Inert particle and catalyst in 9 layers (ε=0.490, d_{cat}=3.67 mm, N_{inert}/N_{cat}=1/2)

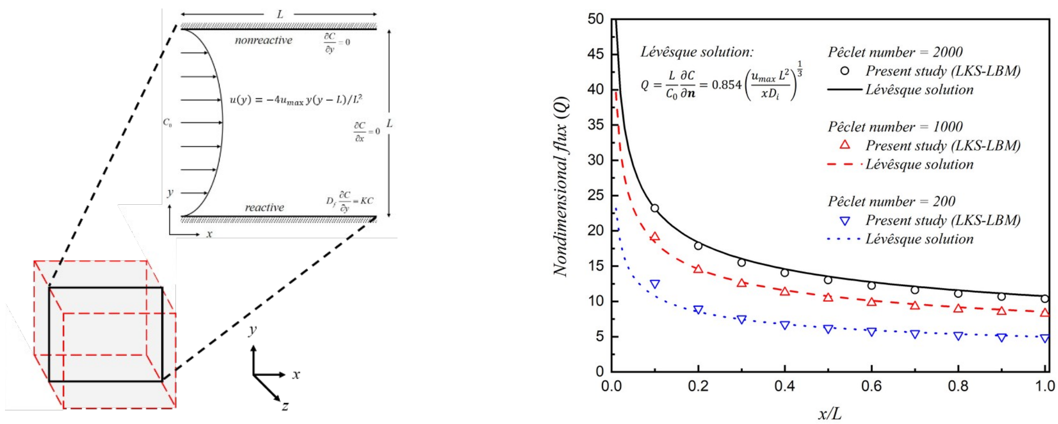

(a) (b)

Fig. 5. (a) Schematic diagram of verification example based on the Lévêsque solution; (b) Comparison of simulated mass-flux by LKS-LBM model (symbols) with the Lévêsque solution (solid line)

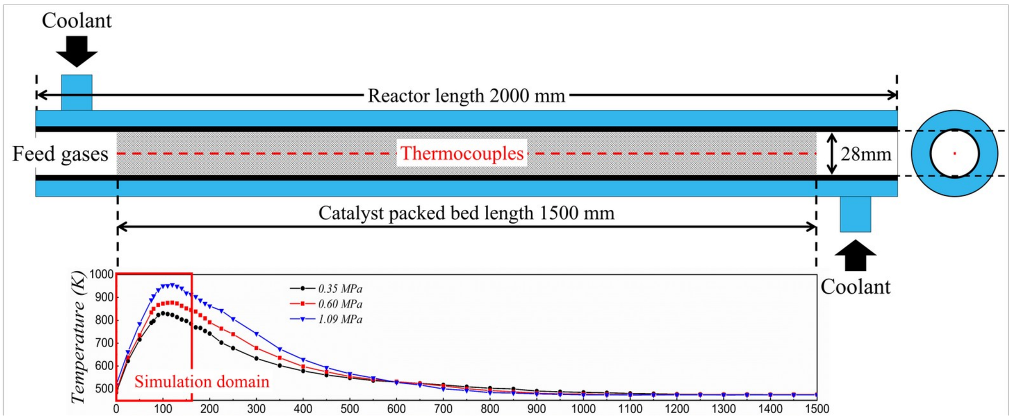

Fig. 6. The schematic diagram of the experiment configuration and measured temperature distribution in the central axial direction

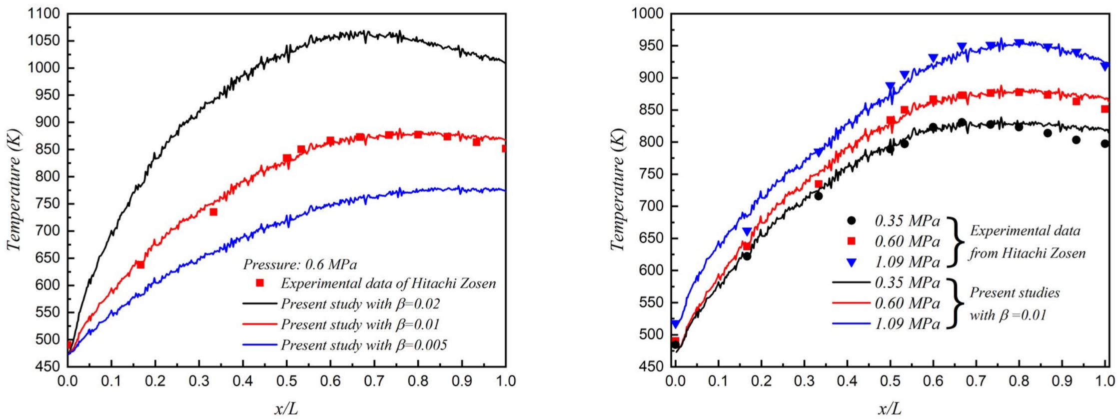

(a) (b)

Fig. 7. (a) Comparison between experimental data and predicted results with three scaling factors in 0.6 MPa; (b) Comparison between the experimental data and predicted results with scaling factor equal to 0.01 under different pressures

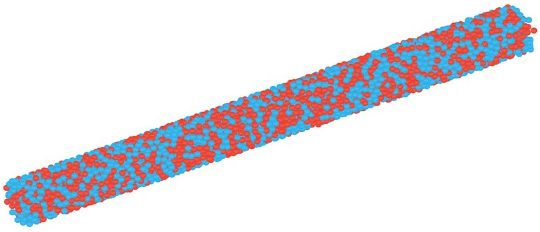

(a)

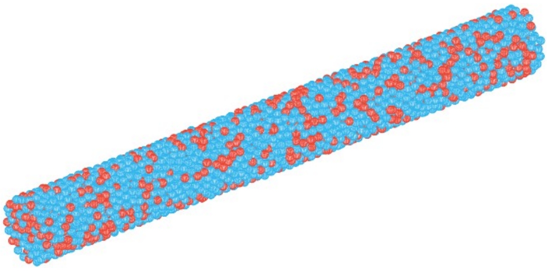

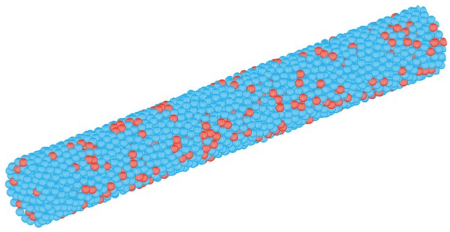

(b) ©

Fig. 8. The bed dilution structure with different inert particle volume fractions:
(a) $V_{inert}/V_{inert+cat}$=50.0%; (b) $V_{inert}/V_{inert+cat}$=33.3%; (c) $V_{inert}/V_{inert+cat}$=16.7%

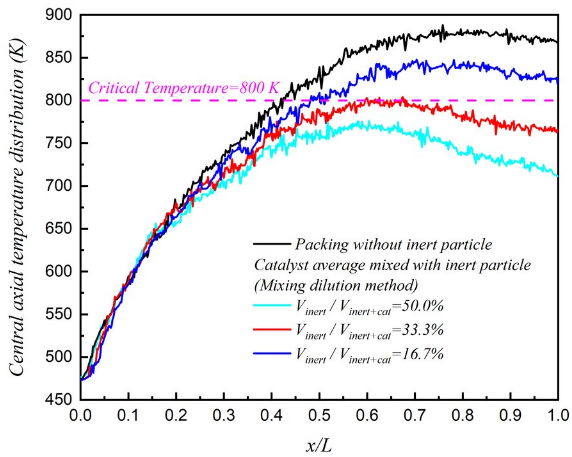

Fig. 9. Dependence of central axial temperature distribution on different inert particle volume fractions

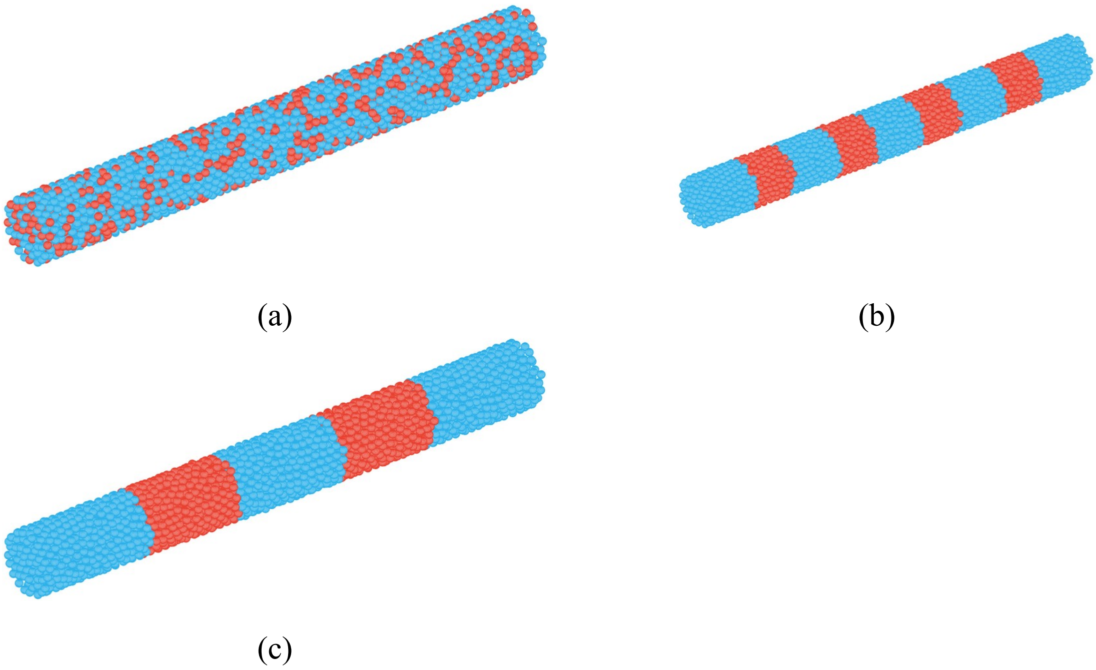

Fig. 10. Schematic diagram of three dilution methods with $V_{inert}/V_{inert+cat}$=33.3%: (a) Catalyst uniformly mixed with inert particle; (b) Inert particle and catalyst in 9 layers; (c) Inert particle and catalyst in 5 layers

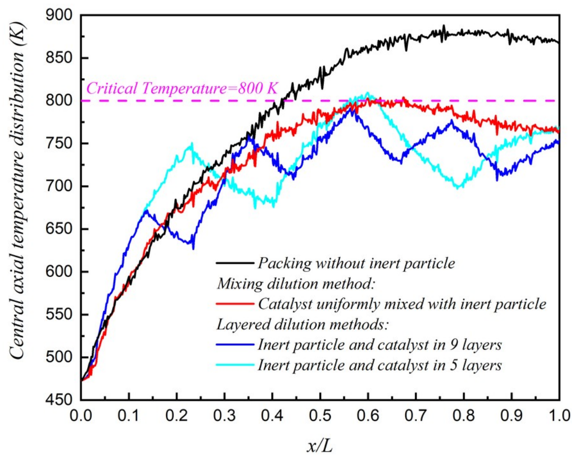

Fig. 11. Dependence of central axial temperature distribution on different inert particle dilution methods along the longitudinal direction

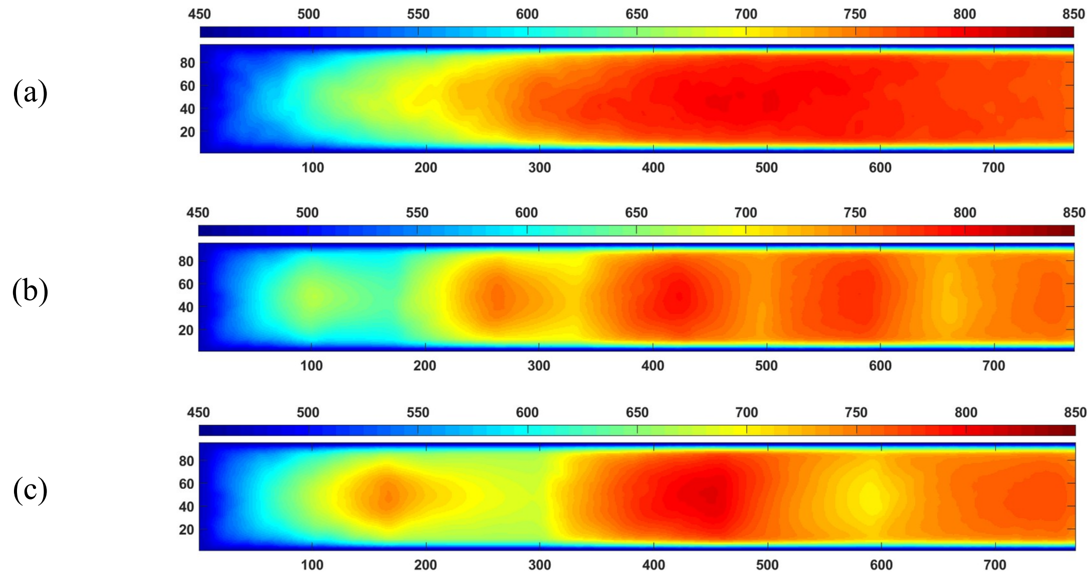

Fig. 12. The temperature distribution in the central cross-section under different inert particle dilution methods: (a) Catalyst uniformly mixed with inert particle; (b) Inert particle and catalyst in 9 layers; (c) Inert particle and catalyst in 5 layers

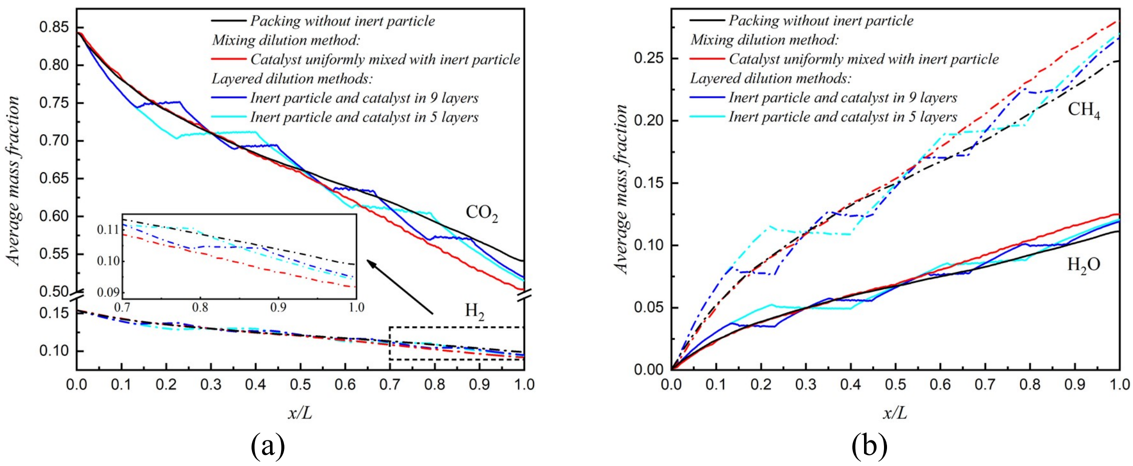

Fig. 13. The average mass fraction distribution of components along the longitudinal direction in different inert particle dilution methods: (a) Reactants (H_2 and CO_2); (b) Products (H_2O and CH_4)

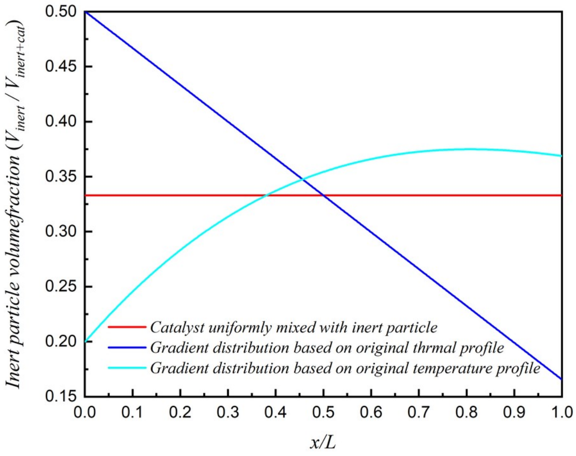

Fig. 14. Inert particle volume fraction distribution along the longitudinal direction for three mixing schemes

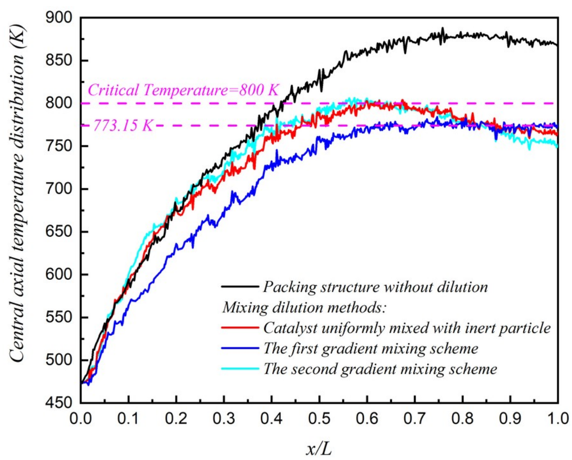

Fig. 15. Dependence of central axial temperature distribution on three kinds of mixing dilution schemes

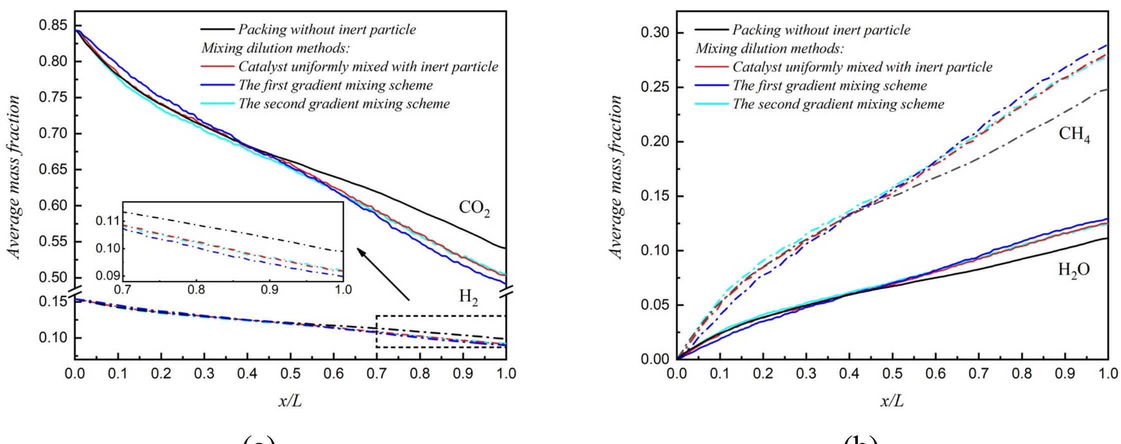

(a) (b)

Fig. 16. The average mass fraction distribution of components along the longitudinal

direction in three kinds of mixing dilution schemes: (a) Reactants (H_2 and CO_2); (b) Products (H_2O and CH_4)

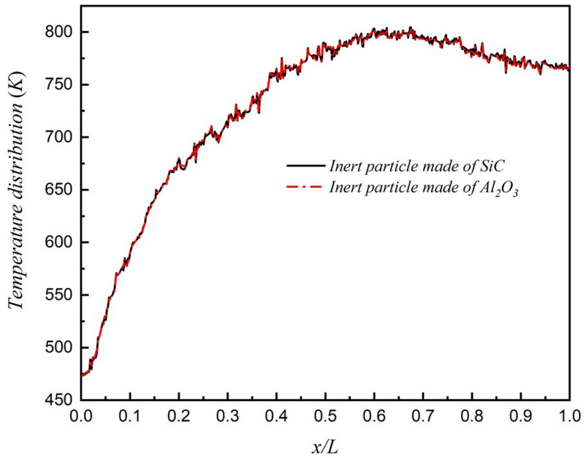

Fig. 17. Dependence of central axial temperature distribution on inert particle thermal conductivity (Al_2O_3: 35 $W \cdot m^{-1} \cdot K^{-1}$ and SiC: 120 $W \cdot m^{-1} \cdot K^{-1}$)

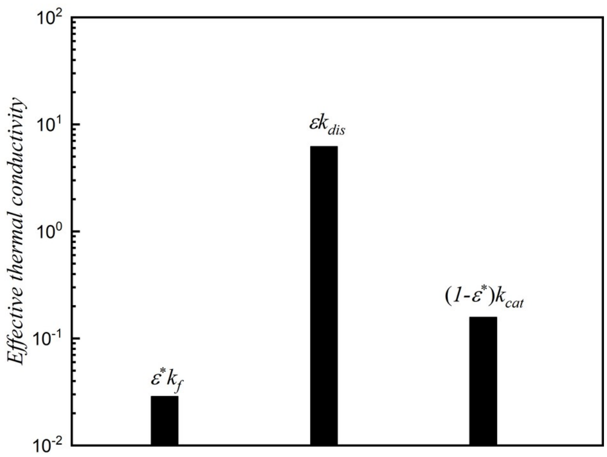

Fig. 18. Comparison of various thermal conductivities without considering inert particle

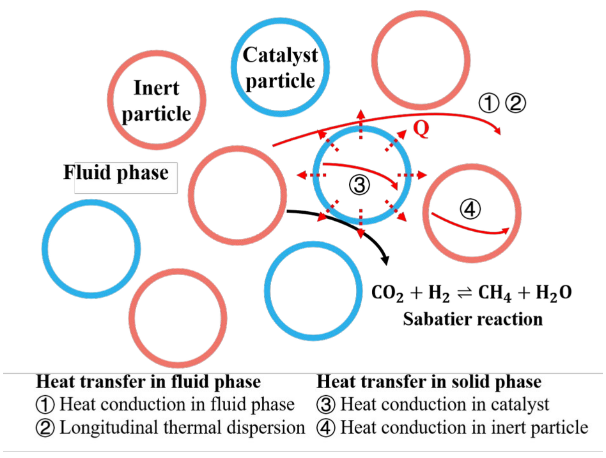

Fig. 19. Schematic diagram of heat transfer in the fluid phase and solid phase considering the bed dilution